

# STUDY OF “DOCTOR BLADE” NANO-CuO PHOTOELECTRODE FOR PERSPECTIVE WATER SPLITTING

## ESTUDIO DE FOTOELECTRODO DE CuO NANOESTRUCTURADO OBTENIDO POR “DOCTOR BLADE” PARA “WATER SPLITTING” PERSPECTIVO

A. BENEDIT-CÁRDENAS<sup>a</sup>, R. CABRERA<sup>a</sup>, A. FUNDORA<sup>b</sup>, B. GONZÁLEZ<sup>b</sup>, C. LAZA<sup>b</sup> AND E. VIGIL<sup>a,b†</sup>

a) Facultad de Física, Universidad de La Habana, 10400 La Habana, Cuba; [evigil@fisica.cu](mailto:evigil@fisica.cu)<sup>†</sup>

b) Instituto de Ciencia y Tecnología de Materiales (IMRE), Universidad de La Habana, 10400 La Habana, Cuba

Recibido 23/4/2019; Aceptado 20/6/2019

In this paper, nano-CuO films, fabricated using the simple “doctor blade” technique, are studied as photoelectrodes in a two-electrode PEC cell for water photolysis. SEM analysis confirm the nanometric size of film grains and the photoelectrode porosity. The photocurrent behavior is studied, particularly, photocurrent transients for non-assisted and assisted water photolysis. Existing defects acting as carrier traps explain the different transient behaviors found. The existence of defects is explored using X-ray diffraction technique and the Williamson-Hall method.

En el presente trabajo, capas de CuO nanoestructurado, fabricadas utilizando la técnica simple de “doctor blade”, se estudian como fotoelectrodos en una celda fotoelectroquímica de dos electrodos para la fotólisis del agua. Los análisis utilizando SEM confirman la dimensión nanométrica de los granos y la porosidad de los fotoelectrodos. Se estudia el comportamiento de la fotocorriente, en particular, sus transitorios, tanto para la fotólisis asistida como la no asistida. Los defectos existentes actuando como trampas de portadores explican los diferentes comportamientos encontrados. La existencia de defectos se analiza utilizando la técnica de difracción de rayos X y el método de Williamson-Hall.

PACS: Nanoporous materials (materiales nanoporosos), 78.67. Rb; photoelectrochemical cells (celdas fotoelectroquímicas), 82.47. Jk; semiconductor-electrolyte (semiconductor electrolito), 73.40. Mr.

### I. INTRODUCTION

Cupric oxide (CuO) is a p-type semiconductor with a monoclinic crystal structure [1] and a direct bandgap of 1.2 eV [2]; for nanostructured CuO direct bandgaps values in the range of 1.4 eV – 1.9 eV have been reported [3–8]. Nevertheless, some researchers have reported indirect bandgaps in the same range [9–11]. All these reported values imply that CuO can convert solar radiation to photocurrent with a good efficiency [12]. Also, for practical use, an inexpensive technique is needed for photoelectrode fabrication because water splitting with solar light requires very large areas. On the other hand, larger CuO gap values have motivated the study of its nanostructured morphologies to split the water molecule (cohesion energy  $E_c = 1.23$  eV) [4–7, 9–11]; since the smaller the nanocrystals, the larger the bandgap due to quantum effects [8, 13].

Photoelectrochemical cells (PEC) with a semiconductor acting as photoelectrode are used for water photolysis or “water splitting” [14–16]. The possibility to split the water molecule depends on the position of the band edges of the semiconductor with respect to water redox levels. The overall band edge positions must straddle the redox potentials of water. This means that the band edge of the conduction band must be above the redox potential of the Hydrogen Energy Reaction (HER) for water splitting without bias. This process is called non-assisted photoelectrolysis or photolysis. If the previous condition is not fulfilled, a bias will be needed for water splitting; in this case, the process is called assisted photoelectrolysis. For CuO,

Chauhan et. al. [17] have reported that a bias is necessary to carry out the photoelectrolysis. But, more recently; other authors have reported that water splitting is possible for nano-CuO photoelectrodes without any bias [4–7, 9–11]. Besides, porous nanostructured photoelectrodes allow a contact area between the semiconductor and the electrolyte larger than the visible flat area. This tridimensional interface improves PEC performance [3, 18, 19].

In the present work nanostructured CuO photoelectrodes are fabricated using the simple “doctor blade” technique [20–22] and their possible use for water photoelectrolysis is analyzed. To the best of our knowledge, this inexpensive technique has not been reported previously to obtain nano-CuO films. The photocurrent behavior for nano-CuO photoelectrodes is analyzed, particularly, photocurrent transients for non-assisted and assisted water photolysis. It is known that defects acting as carrier traps decrease the process efficiency in assisted and non-assisted water splitting [23]. The existence of defects is explored further processing X-ray diffraction patterns with the Williamson-Hall method [24, 25].

### II. MATERIALS AND METHODS

#### II.1. CuO films fabrication

CuO films were prepared using Aldrich nano-powder (particle diameter < 50 nm). First, the nanopowder was mortar disaggregated. Then, 2 mL of a 40 % distilled water and 60 % ethylene glycol solution per gram of CuO were used to prepare a nano-CuO colloidal suspension. This suspension

was deposited on optical glass, as well as, on conducting glass FTO Tec-15 by “doctor blading”. Air drying of the CuO layer was followed by a heat treatment in air for an hour at  $T = 80^{\circ}\text{C}$  to avoid brisk water evaporation. Afterwards, temperature was raised to  $500^{\circ}\text{C}$  for another hour to eliminate organics and to produce nanocrystals necking. This is a usual procedure in DSSC to favor charge conduction between nanocrystals [26]. Three samples were fabricated with this technique: NP 1, NP 2 and NP 3.

### II.2. PEC cell photocurrent measurements

CuO films were evaluated as photoelectrodes inside a two-electrode photoelectrochemical cell (PEC) system (dimensions  $2.5 \times 3.3 \times 4.0 \text{ cm}^3$ ) as described elsewhere [27]. The CuO/FTO film acted as photoelectrode, a platinum wire as counter-electrode and distilled water as electrolyte. Photocurrent was measured in a lab-developed set-up with an Agilent 34410A multimeter attached to a PC. A  $100 \text{ mW/cm}^2$  light intensity on the photoelectrode was established employing a halogen lamp, focusing lenses and a calibrated photodiode. The PEC and its electrical contacts were placed inside a Faraday box. Measurements were taken automatically using a Labview program which allows: to control the amperemeter, to plot photocurrent values in real time and to save all the data. Photocurrent behavior for light-on and off cycles was registered with and without an applied voltage of 1.2 V.

### II.3. Morphological and structural analysis

Scanning electron microscopy (SEM) was performed with a JEOL 7600 instrument and 10kV acceleration voltage. Secondary electrons were used for surface imaging. The nano-powder and the prepared films were analyzed to detect the existence of defects using X-ray diffraction (XRD). Experiments were performed with an Empyrean Panalytical diffractometer, X' Pert3 Powder. XRD patterns cover the range  $10^{\circ} < 2\theta < 90^{\circ}$ , where  $\theta$  is the Bragg reflection angle. Cu  $K_{\alpha}$  radiation,  $\lambda = 1.5406 \text{ \AA}$ , was used for all XRD experiments.

## III. RESULTS AND DISCUSSIONS

### III.1. Scanning electron microscopy

The SEM image in Fig. 1 shows that the film is porous and formed by nanograins. This is advantageous because porosity gives rise to a tridimensional semiconductor/electrolyte interface with an area much larger than the visible photoelectrode area. This favors photocurrent increase. On the other hand, carriers must follow a tortuous path to the external contact and they must cross multiple interfaces between nanograins where recombination losses occur.

### III.2. Photocurrent measurements

It is important that energy levels requirements for water splitting are fulfilled for “doctor bladed” films since when illuminated a current always exists without any bias. Fig. 2 shows an example of photocurrent versus time for zero bias; transients are observed when light is turned on and also when it is turned off. The behavior of these transients is analyzed and related to recombination centers.

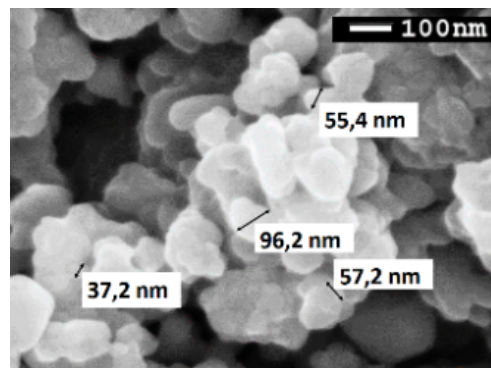


Figure 1. SEM image of a fabricated films.

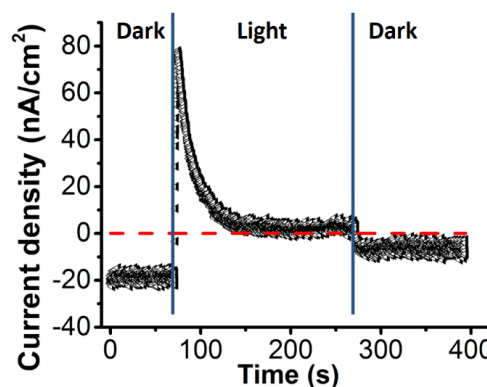


Figure 2. Photocurrent density vs time at zero bias. Transients for light-on and light-off conditions are observed.

Fig. 3 shows photocurrent transients for samples NP 1, NP 2 and NP 3, for bias voltage  $V = 0 \text{ V}$  and  $V = 1,2 \text{ V}$ . Figs. 3a and 3c allow to compare photocurrent values for these bias voltages during light-on periods. Photocurrent values are higher than one order of magnitude when voltage is applied. This indicates that bias favors the relative positions of CuO bands with respect to the electrolyte redox levels. One can observe in Fig. 3b that without an applied voltage and without light a negative current exists in all samples. Therefore, in the dark, the porous-nanostructured CuO photoelectrodes under study show a small electromotive force effect. This behavior has been previously reported for CuO [4,5,7,28]. It has been associated with weak chemical stability or charge accumulation in trap centers located at CuO interphases. No change was observed or registered for samples after repeated measurements, so, weak stability was discarded as the reason for negative dark current. The dark current must be due to accumulated charge release.

For both, non-assisted and assisted photoelectrolysis, photocurrent light-on and light-off transients were fitted with (1) and (2), respectively.

$$I(t) = I_{dark} + A \left(1 - e^{-\frac{t}{T_1}}\right) + B \left(1 - e^{-\frac{t}{T_2}}\right) + Q \left(1 - e^{-\frac{t}{T_3}}\right), \quad (1)$$

$$I(t) = I'_{dark} + Ae^{-\frac{t}{T_1}} + Be^{-\frac{t}{T_2}} + Qe^{-\frac{t}{T_3}}. \quad (2)$$

These linear combinations of exponentials have coefficients  $A$ ,  $B$  and  $Q$  and characteristic times  $T_1$ ,  $T_2$  and  $T_3$ .  $I_{dark}$  and  $I'_{dark}$  are the current values in the dark. The second, third and fourth term in equations 1 and 2 have the sign of the coefficients  $A$ ,  $B$  and  $Q$ , respectively. A negative coefficient means that the photocurrent decreases and viceversa.

Table 1 shows parameter values obtained by fitting (1) (light-on) for samples NP 1, NP 2 and NP 3. The values of are always positive; i.e., the photocurrent increases. The values of and change from negative to positive when the bias changes from 0 V to 1.2 V. Therefore, the effect associated

with  $T_2$  and  $T_3$  causes a photocurrent decrease when no bias is applied and an increase when a bias of 1.2 V is applied.

Figs. 3b and 3d show current transients when light is turned off. These figures show experimental values, as well as, those that result from fitting them with (refeq2). In this case, the values for the characteristic time are:  $0.5\text{ s} < T_1 < 0.6\text{ s}$ ;  $8,0\text{ s} < T_2 < 8,5\text{ s}$  and  $24,5\text{ s} < T_3 < 25,0\text{ s}$ . These values are similar to those that correspond to  $T_1$ ,  $T_2$  and  $T_3$  for light-on transients (see Table 1). Similar values indicate that the same processes are involved during light-on and light-off transients.

The  $A$  coefficient term can be assigned to light-generated free carriers initially reaching the FTO contact. The delayed increase, shown in Fig. 3a and 3c and characterized by  $T_1$ , indicates that carriers do not reach the FTO contact immediately. Most probably, transport occurs by trapping and detrapping as has been already reported in nanostructured solar cells [29,30].

Table 1. Parameters in (1) for light-on photocurrent transients.

Samples	Bias	$I_{dark}$ (nA/cm <sup>2</sup> )	$T_1$ (s)	$A$ (nA/cm <sup>2</sup> )	$T_2$ (s)	$B$ (nA/cm <sup>2</sup> )	$T_3$ (s)	$Q$ (nA/cm <sup>2</sup> )
NP 1	0 V	-89	0.4	240	8.0	-91	25.2	-91
	12 V	495	0.6	291	8.0	96	25.0	27
NP 2	0 V	-9	0.7	51	8.0	-3	25.0	-40
	12 V	425	0.5	454	8.0	72	25.0	6
NP 3	0 V	-19	0.7	115	8.2	-44	25.0	-51
	12 V	442	0.5	564	8.2	88	25.0	18

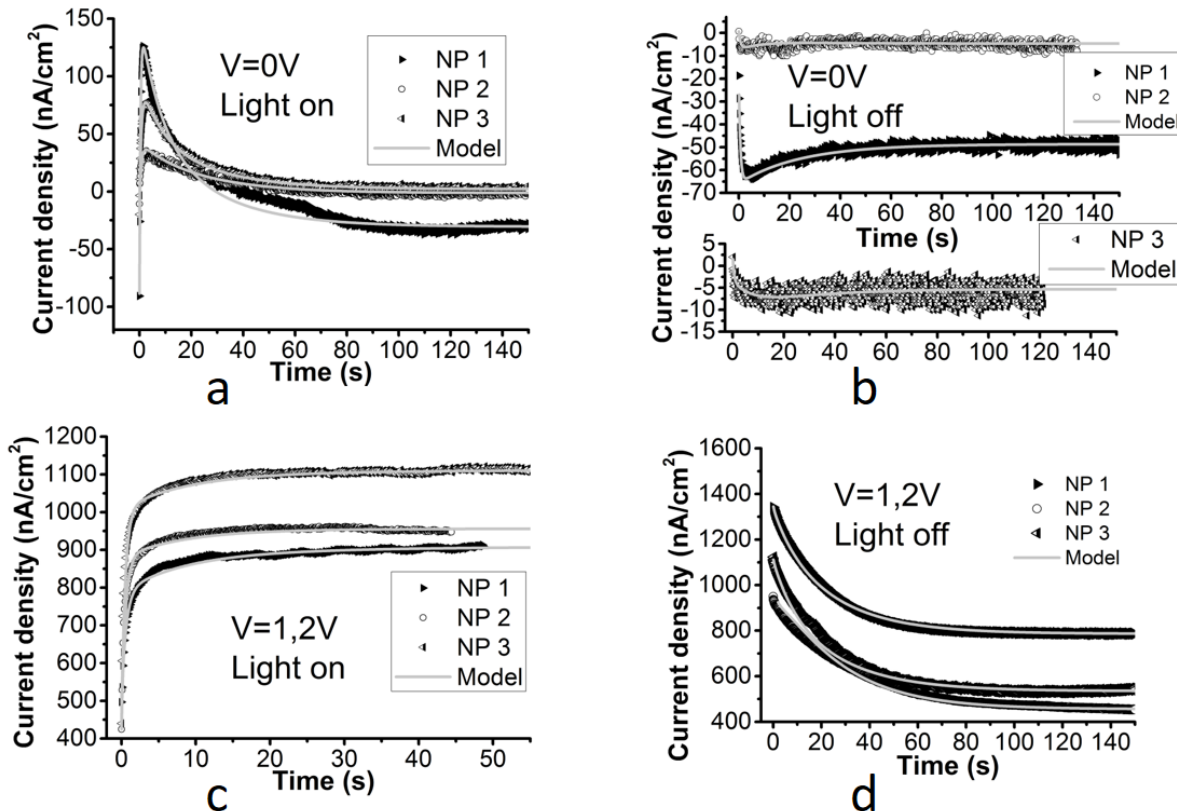


Figure 3. Photocurrent transients for samples NP 1, NP 2 and NP 3. Experimental values are shown together with continuous line corresponding to (1) and (2). a) light-on, zero applied bias ( $V=0\text{ V}$ ) b) light-off, zero applied bias ( $V=0\text{ V}$ ). c) light-on, applied bias,  $V=1.2\text{ V}$  d) light-off, applied bias,  $V=1.2\text{ V}$ .

The values of coefficient and shown in Table 1 can be explained through the existence of traps with energy values in the bandgap of the semiconductor. Fig. 4a shows a band scheme with one trap level and it applies to “light-off” condition without bias. In this situation the electron trap (above the Fermi level) is mostly empty. When the photoelectrode is illuminated and free electrons generated (Fig. 4b) the electron trap captures them from the conduction band. Therefore, when the photoelectrode is illuminated with no voltage applied, the electron trap causes photocurrent to decrease, because some electrons are trapped and cannot behave as free carriers.

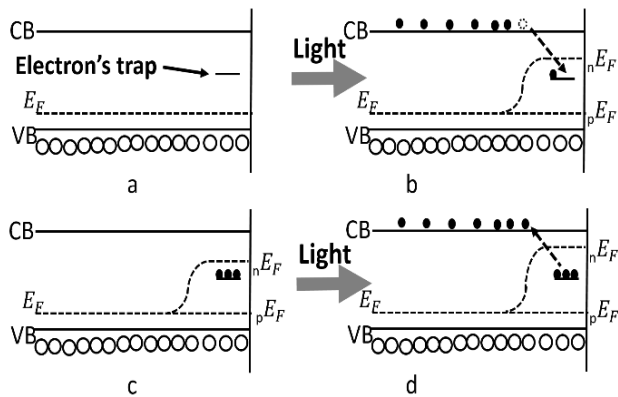


Figure 4. Band diagrams showing trap levels a) dark condition without an applied bias b) light-on condition without an applied bias c) dark condition with an applied bias d) light-on condition with an applied bias.

When a high enough bias is applied, the quasi-Fermi level can be above the electron trap level; therefore, this level will be mostly filled in the dark (see Fig. 4c). When the photoelectrode is illuminated (Fig. 4d), since traps are mostly filled, they are limited in capturing electrons and may inject electrons to the conduction band. (contrary to the non-assisted photoelectrolysis situation). Accordingly, an electron trap can decrease the photocurrent in non-assisted photoelectrolysis and increase the photocurrent in assisted photoelectrolysis.

Therefore, existing electron traps in the sample can be associated with the terms having the  $B$  and  $Q$  coefficients; i.e. to the processes characterized by  $T_2$  and  $T_3$ . When no bias is applied, the values of the coefficients  $B$  and  $Q$  are negative (see Table 1), which means that there is a photocurrent decay (see Fig. 3a), in agreement with the behavior of the electron trap in Fig. 4b. When a bias is applied the values of the coefficients  $B$  and  $Q$  are positive (see Table 1), which means that the photocurrent increases (see Fig. 3c), in agreement with the behavior of the electron trap in Fig. 4d. It was impossible to fit the experimental curves to a sum of only two exponentials; three terms were necessary. This means that there are two trap levels with characteristic times  $T_2$  and  $T_3$ , respectively. Therefore, photocurrent transients show the existence of more than one trap level and their deleterious effect on photocurrent. It is known that structural volume defects could create strains and they could act as carrier traps.

### III.3. XRD analysis

The previous photocurrent analysis shows the existence of traps in the samples [31]. These can be due to volume or surface defects. Surface defects cause carrier losses at the surface of the nano-crystal where they are created but also during their transport to the contact. This is due to the barriers existing between crystallites and between nanograins; even though, usual heat treatment decreases the last ones by producing “necking” between nanocrystals. Strain-defects in the samples were analyzed applying the Williamson-Hall method to XRD patterns [32–34]. Fig. 5a shows CuO line pattern (from the version of 2011 of ICSD, collection code: 628616). Figs. 5b and 5c show nanopowder and films XRD patterns, respectively. For Williamson-Hall analysis, the diffraction peaks were fitted with a PseudoVoigt function in order to find the FWHM (full width at half maximum) of each one.

The crystallite size  $L$ , and the coefficient characterizing strain distribution  $\epsilon$ , were calculated using Williamson-Hall method. This takes into account the contribution of both, the crystallite size and the strain distribution, to the peak width at half the maximum intensity (FWHM) [35], which is equal to

$$FWHM(2\theta) = 4\epsilon \frac{\sin \theta}{\cos \theta} + \frac{k\lambda}{L \cos \theta'} \quad (3)$$

where  $\theta$  is the Bragg angle, the peak width at half the maximum intensity (FWHM) is obtained from diffraction peaks in an intensity vs  $2\theta$  plot,  $\lambda$  is the wavelength and  $k$  is the Scherrer’s constant ( $k = 0.90$ ). For the Williamson-Hall plots shown in Figs. 5d and 5e, small peaks with poor fitting parameters according to PseudoVoigt analysis were discarded, as well as, two pairs of unresolved peaks: (111) with (200) plus (-222) with (004). Figs. 5d and 5e show the Williamson-Hall plots for the nano-powder and films, respectively. Values for the crystallite size and the coefficient characterizing strain distribution obtained from them are shown in Table III.3.

Table 2. Parameters obtained with the Williamson-Hall method.

	Powder	Film
Crystallite size (nm)	$12.6 \pm 0.4$	$20 \pm 4$
strain coefficient	$-(7 \pm 2) \times 10^{-4}$	$(1.0 \pm 0.8) \times 10^{-3}$

Comparison of crystallite value in Table III.3 with grain dimensions in Fig. 1 indicate that there are very few crystallites in a nanograin. According to values in Table III.3, crystallite size in the film increases with respect to its nanopowder size. This change can be associated with the heat treatment at  $500^\circ\text{C}$  during one hour. Heat treatment originates necking between nanograins [26] which increases their sizes.

Besides, according to (3), the slope of the line in Fig. 5e for the nano-CuO film is equal to four times the strain coefficient  $\epsilon$ . Its value ( $m = 0.00384$ ) is very close to zero; i.e. to no strain at all. Therefore, strain distribution contributes little to FWHM value. This points to a small number of strain-defects in the nanocrystal volume.

Considering this and that there are very few crystallites in a nanograin, a high number of defects in the disordered surfaces of nanograins must be the origin of the large number of traps responsible for low photocurrent values obtained. A low number of defects in the film nanocrystals supports Dimopoulos et. al. [36] who reports a carrier diffusion length of 40 nm in nanostructured CuO. This value is high enough so as to limit recombinations inside the nanocrystals.

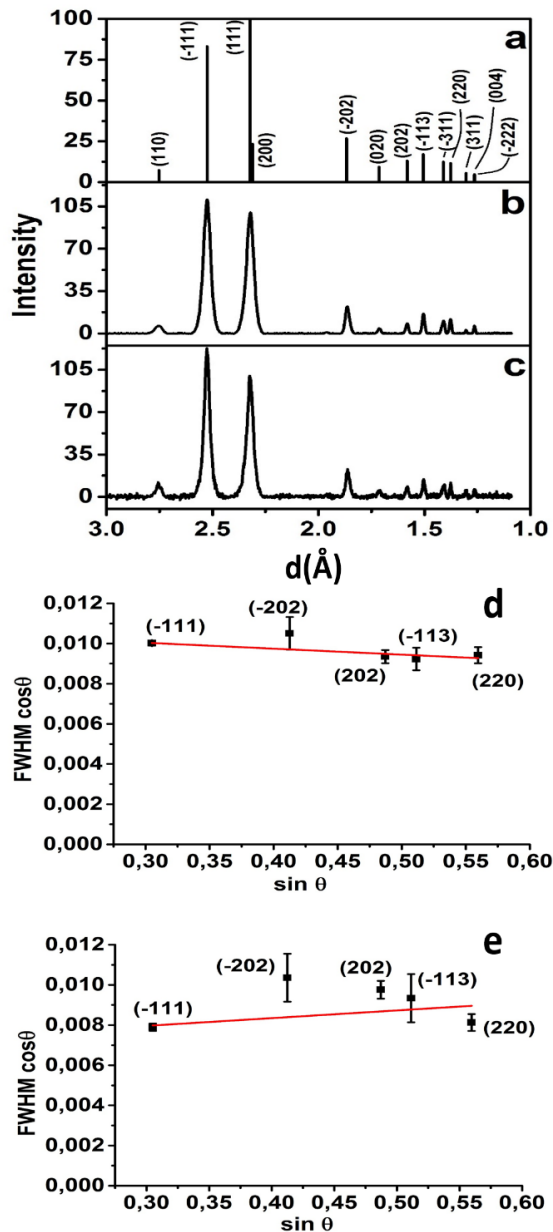


Figure 5. XRD analysis a) CuO line pattern (ICSD 628616) b) nanopowder XRD pattern c) film XRD pattern d) Williamson-Hall plot for nanopowder e) Williamson-Hall plot for films.

#### IV. CONCLUSIONS

CuO nanostructured photoelectrodes were fabricated using the inexpensive and simple “doctor blade” technique. SEM analysis showed the nanostructure morphology and porosity of deposited films. These are important characteristics to create a semiconductor-electrolyte tridimensional interface

with an area much larger than the visible photoelectrode area. Photocurrent registered with zero bias corroborates that the non-assisted photoelectrolysis of water is possible with the “doctor blade” fabricated CuO films. Photocurrent values for voltage bias  $V = 1.2$  V are one order of magnitude higher. This indicates that voltage bias favors the relative position of the CuO bands with respect to the electrolyte redox levels.

Photocurrent transients were fitted with a linear combination of three exponentials plus a dark current term. Three characteristic times were found for light-on, as well as, light-off transients; which are explained by the same mechanisms: carrier transport to the FTO contact and electron capture by two different trap centers.

Williamson-Hall analysis of XRD patterns indicate that strain defects practically do not exist in the nanocrystal volume. Therefore, the trap centers that affect photocurrent behavior must be surface and interface defects.

#### V. ACKNOWLEDGMENTS

We thank Dr. Ernesto Estévez for very useful discussions on diffractograms and their processing. And we thank Dr. Osvaldo de Melo for scanning electron microscopy experiments.

#### REFERENCES

- [1] J.B. Forsyth and S. Hull, *J. Phys.: Condens. Matter* **3**, 5257, (1991).
- [2] Handbook of Chemistry & Physics 71st Edition. Michigan: CRC Press; (1990).
- [3] X.D. Wang, Y.F. Xu, B.X. Chen, N. Zhou, H.Y. Chen, D.B. Kuang and C.Y. Su, *ChemSusChem* **9**(20), 3012 (2016).
- [4] A. Ray, I. Mukhopadhyay, R. Pati, Y. Hattori, U. Prakash and Y. Ishii, *J. Alloys Compd.* **695**, 3655 (2017).
- [5] M. Patel, H.S. Kim, D.B. Patel and J. Kim, *J. Mater. Res.* **31**, 3205 (2016).
- [6] J.G. Lee, D.Y. Kim, J.H. Lee, M.W. Kim, S. An and H.S. Jo, *ACS Appl. Mater. Interfaces* **8**, 15406 (2016).
- [7] W. Septina, R.R. Prabhakar, R. Wick, T. Moehl and S.D. Tilley, *Chem. Mater.* **29**, 1735 (2017).
- [8] O. Langmar, C.R. Ganivet, P. Schol, T. Scharl, G. de la Torre and T. Torres, *J. Mater. Chem. C* **6**, 5176 (2018).
- [9] A. Mahmood, F. Tezcan and G. Kardas, *Int. J. Hydrogen Energy* **42**, 23268 (2017).
- [10] A. Kushwaha, R.S. Moakhar, G.K.L. Goh and G.K. Dalapati, *J. Photochem. Photobiol., A* **337**, 54 (2017).
- [11] M. Einert, T. Weller, T. Leichtweis, B.M. Smarsly and R. Marschall, *ChemPhotoChem* **1**, 326 (2017).
- [12] W. Shockley and H.J. Queisser, *J. Appl. Phys.* **32**, 510 (1961).
- [13] Q. Zhang, K. Zhang, D. Xu, G. Yang, H. Huang and F. Nie, *Prog. Mater. Sci.* **60**, 208 (2014).
- [14] I. Roger, M.A. Shipman and M.D. Symes, *Nat. Rev. Chem.* **1**, 0003 (2017).
- [15] C. Jiang, S.J.A. Moniz, A. Wang, T. Zhang and J. Tang, *Chem. Soc. Rev.* **46**, 4645 (2017).

- [16] J. Joy, J. Mathew and S.C. George, *Int. J. Hydrogen Energy* **43**, 4804 (2018).
- [17] D. Chauhan, V.R. Satsangi, S. Dass and R. Shrivastav, *Bull. Mater. Sci.* **29**, 709 (2006).
- [18] Y.J. Jang, J.W. Jang, S.H. Choi, J.Y. Kim, J.H. Kim and D.H. Youn, *Nanoscale*, **7**, 7624 (2015).
- [19] H.B. Oh, H. Ryu and W.J. Lee, *J. Alloys Compd.* **620**, 55 (2015).
- [20] M.K. Nazeeruddin, A. Kay, I. Rodicio, R. Humphry-Baker, E. Mueller and P. Liska, *J. Amer. Chem. Soc.* **115**, 6382 (1993).
- [21] K. Kalyanasundaram and M. Grätzel, *Coord. Chem. Rev.* **177**, 347 (1998).
- [22] M.H. Habibi and M.H. Rahmati, *Spectrochim. Acta, Part A* **137**, 160 (2015).
- [23] L. Zhang, H.H. Mohamed, R. Dillert and D. Bahnemann, *J. Photochem. Photobiol., C* **13**, 263 (2012).
- [24] A.A. Akl, S.A. Mahmoud, S.M. Al-Shomar and A.S. Hassanien, *Mater. Sci. Semicond. Process.*, **74**, 183 (2018).
- [25] P.M. Shafi and A.C. Bose, *AIP Adv.* **5**, 057137 (2015).
- [26] S. Nakade, M. Matsuda, S. Kambe, Y. Saito, T. Kitamura and T. Sakata, *J. Phys. Chem. B* **106**, 10004 (2002).
- [27] I. Zumeta, R. Espinosa, J.A. Ayllón, X. Domènech and X. Rodri, *Sol. Energy Mater. Sol. Cells* **76**, 15, (2003).
- [28] J. Oh, H. Ryu, W.J. Lee and J.S. Bae, *Ceram. Int.* **44**, 89 (2018).
- [29] G. Schlichthörl, N.G. Park and A.J. Frank, *J. Phys. Chem. B* **103**, 782 (1999).
- [30] C.R. McNeill, I. Hwang and N.C. Greenham, *J. Appl. Phys.* **106**, 024507 (2009).
- [31] R. van de Krol, *Principles of Photoelectrochemical Cells. Photoelectrochemical Hydrogen Production* (Boston, Springer, 2012).
- [32] V.P. Singh, D. Das and C. Rath, *Mater. Res. Bull.* **48**, 682 (2013).
- [33] B. Choudhury, P. Chetri and A. Choudhury, *J. Exp. Nanoscience* **10**, 103 (2015).
- [34] G.K. Williamson and W.H. Hall, *Acta Metall.* **1**, 22 (1953).
- [35] E.J. Mittemeijer and U. Welzel, *Modern Diffraction Methods* (John Wiley & Sons, New York, 2013).
- [36] T. Dimopoulos, A. Peić, P. Müllner, M. Neuschitzer, R. Resel and S. Abermann, *J. Renew. Sustain. Energia* **5**, 011205 (2013).

---

This work is licensed under the Creative Commons Attribution-NonCommercial 4.0 International (CC BY-NC 4.0, <http://creativecommons.org/licenses/by-nc/4.0>) license.

